Nano Energy 33 (2017) 1–11

Contents lists available at ScienceDirect

Nano Energy

journal homepage: www.elsevier.com/locate/nanoen

Development of battery-free neural interface and modulated control of tibialis anterior muscle via common peroneal nerve based on triboelectric nanogenerators (TENGs)

Sanghoon Lee[a,b,c,d], Hao Wang[a,b,c,d], Qiongfeng Shi[a,b,c,d], Lokesh Dhakar[a,c], Jiahui Wang[a,b], Nitish V. Thakor[b,e,f], Shih-Cheng Yen[a,b,c], Chengkuo Lee[a,b,c,d,e,*]

[a] *Department of Electrical and Computer Engineering, National University of Singapore, 4 Engineering Drive 3, Singapore 117583, Singapore*
[b] *Singapore Institute for Neurotechnology (SINAPSE), National University of Singapore, Singapore 117456, Singapore*
[c] *Center for Intelligent Sensors and MEMS, National University of Singapore, 4 Engineering Drive 3, Singapore 117576, Singapore*
[d] *NUS Suzhou Research Institute (NUSRI), Suzhou, Industrial Park, Suzhou 215123, PR China*
[e] *Graduate School for Integrative Science and Engineering, National University of Singapore, Singapore 117456, Singapore*
[f] *Johns Hopkins University, Biomedical Engineering, Baltimore, MD 21205, USA*

ARTICLE INFO

Keywords:
Flexible electronics
e-Skin
Implantable bioelectronics
Neural interface
Selective stimulation
Triboelectric nanogenerator (TENG)

ABSTRACT

Flexible and stretchable electronics, also known as e-skin, have been a technology to create diversified sensors and wearable devices. Implantable bioelectronics have recently been recognized as a promising research field to modulate biological signals and treat many diseases and pathological conditions. The marriage of two technologies gives us a new cutting-edge research area, i.e., implantable flexible electronics. While strain sensors, ECG sensors, pH sensors, temperature sensors and LED chips have been integrated together as a novel platform for measuring physiological signals, one of critical challenges for long-term use of such devices is a reliable power source with sound output power. To support operation of the implantable bioelectronics, triboelectric nanogenerators (TENGs) have recently been explored, as a promising technology to harvest energy, as the concept of scavenging human body energy into useful electrical power.

In this work, we investigate stacked TENGs with output voltage of 160 $V_{p\text{-}p}$ and a short circuit current of 6.7 μA as a potential power source for neural stimulation using flexible and adjustable neural interfaces. To advance a generic design of flexible neural interfaces which is good at sciatic nerve recording and stimulation, we optimize a new flexible sling electrode and successfully achieve neural signal recording with different amplitudes and latencies. More importantly, successful selective stimulation achieved in this work proves that the flexible sling electrode is a good generic neural interface. We demonstrate direct stimulation of a sciatic nerve and a common peroneal nerve in rats by the TENGs connected with the suggested interface and a pair of Pt/Ir wires, respectively, while monitoring muscle signals. The muscle contraction can be controlled by the operation of the TENGs. This prove-concept result indicates that this technology could be the way of realizing battery-free wearable neuromodulators in the future.

1. Introduction

Implantable bioelectronics have recently emerged as a powerful way to monitor biological signals and treat diseases such as pacemakers, deep brain stimulators, and neuromodulators [1–3]. The enormous progress attributed to the development of flexible/stretchable electronics, which enables the integration of various kinds of biosensors, actuators and energy storage elements, has opened up a new research field [4–8]. Meanwhile, using e-skin technology to craft soft and stretchable implantable/wearable medical devices, it has also provided a better interface to the human organs, blood vessels and neural branches. By using these flexible implantable bioelectronics to achieve more sensitive and accurate bio-signal recording and stimulation, we have new ways of enabling electroceuticals [9–11]. One of critical challenges for long-term use of such devices is a reliable power source with sound output power. Some feasible solutions have been investigated including external energy sources, which are out of body and provides energy to the devices via wired [3] and wireless [12–14] communication, and implantable batteries that normally require recharge or replacement [15,16]. The concept of scavenging human

* Corresponding author at: Department of Electrical and Computer Engineering, National University of Singapore, 4 Engineering Drive 3, Singapore 117583, Singapore.
E-mail address: elelc@nus.edu.sg (C. Lee).

http://dx.doi.org/10.1016/j.nanoen.2016.12.038
Received 23 October 2016; Received in revised form 17 December 2016; Accepted 17 December 2016
Available online 10 January 2017
2211-2855/

body energy into useful electrical power by various mechanisms has been explored as an alternative way to support operation of such implantable bioelectronics. For example, thermal energy from the body heat by thermoelectric device [17–21], mechanical energy from arterial dilation and contraction by piezoelectric device [22–25], and muscle contraction by electromagnetic device [26] have been reported. Among the devices of mechanical energy harvesting, triboelectric nanogenerators (TENGs) have recently been proposed as a promising technology [27–38]. The TENGs work on the principle of contact electrification [39–41] between two materials coupled with electrostatic induction providing advantages of lower cost, a wider range of material choice (flexible and biocompatible materials) [42–44], easy fabrication, and high power output by stacking of multiple layers [45,46] as compared to other energy generators. Recently, some *in vivo* demonstrations of energy harvesting from heart beat [47–49] and muscle contraction [50] showed the possibility of using the TENGs as an implantable power source. Moreover, biodegradable TENGs were studied totally eliminating the concern of post-surgery for the extraction of the device [51]. Without looking into physiological basis and relationship between various muscle bundles and a sciatic nerve, Zhang et al. demonstrated strokes of a separated frog leg attached with a microneedle electrode array (MEA) on the sciatic nerve which was biased by a TENG [52]. Although the MEA used in this work is relatively invasive to nerves as well as the design is not good for long-term use and selective stimulation for activation of different muscles in a control manner, it opens an attractive research direction of TENGs for direct stimulation of a peripheral nerve.

On the other hand, the central nervous system (CNS) and peripheral nervous system (PNS) send and receive bio-signals from different parts of the body to coordinate body's voluntary and involuntary actions. Thus, continuous monitoring of bio-potentials generated from the nervous system is critically important in healthcare and can help clinicians to diagnose and even treat diseases such as epilepsy, heart disease (arrhythmia and hypertension), and Parkinson's. The e-skin technology has opened a new research filed of using ultrathin, flexible and stretchable electronics to measure bio-signals and other electrical, mechanical, and optical information such as impedance, strain and pressure, etc [53–60]. High density and multiplexed electrode arrays consisted of active circuitry have been demonstrated to conformally contact the surface of the cortex and to record sleep spindles, visual evoked responses, and micro/macro seizures in living animal models [61,62]. In peripheral nerves, flexible MEA have enabled the implementation of penetrating interfaces with fascicular and sub-fascicular selectivity. Intra-fascicular interfaces are inserted transversally or longitudinally regarding the long axis of the sciatic nerve. Neural cuffs are tubular devices placed around the epineurium of a whole nerve and have electrodes on their inner surface. The conceptual drawings of these neural electrodes are shown in Fig. 1, such as extra-neural (cuff and FINE) (Fig. 1a) [63–66], penetrating (USEA) (Fig. 1b) [67–69], intra-fascicular (LIFE and TIME) (Fig. 1c) [70–72], and regenerative electrodes [73–76]. Among these four types of electrodes, extra-neural electrodes have been most broadly used for clinical applications thanks to their non-invasive approach and easy implantation. However, the use of extra-neural cuff electrodes typically carries a high risk of damaging the nerve if the inner walls are too close to the nerve. A flat interface nerve electrode (FINE) as an advanced version of the cuff interface was studied in recording of human median and ulnar nerves [66] as well as stimulation of human tibial and common peroneal nerve to activate important muscles for neuroprosthesis [77]. Adaptive flexible ribbon electrodes capable of electroneurogram (ENG) recordings on specific small branches of a sciatic nerve were recently demonstrated by achieving close contact with nerve surfaces without applying too much pressure to the nerve [78,79]. Approaching such small nerves will reduce the number of contacts required as well as enhance selectivity of recording or stimulation. In particular, the common peroneal nerve primarily innervates ankle dorsiflexors, such as tibialis anterior, extensor digitorum longus, extensor hallucis longus, and ankle evertors [77]. Also, it may be useful in direct physiotherapy of the drop foot [80]. However, application of the neural ribbon electrodes meets some constrains during the implantation. They have to be wrapped around a nerve in surgical implantation, which sometimes is not feasible within limited space (Fig. 1d). This may not always be possible if space is limited. In addition, it is difficult to handle the active electrodes upon the nerve and to control the position of the electrodes on the nerve for selective stimulation or optimal recording [78,79]. Chronic high-quality neural recording may also be challenging due to the lack of tripolar or bipolar configurations for this design. For clinical neuromodulation applications, reliable neural interfaces closely attached to nerves without causing damage should provide selective stimulation or recording of nerves. Moreover, such TENGs as an alternative energy source should provide electric charge to a nerve for reliable activation of targeted muscles.

With the development demonstrated so far, we demonstrate a developed and optimized TENG as a potential power source to neural interfaces based on flexible electronics technology. Also, we demonstrate a flexible and adjustable neural interface for selective nerve recording and stimulation with good electrical contact but minimal pressure on rat sciatic nerves. Towards next step of clinical applications, we demonstrate direct stimulation using TENGs combined with neural interfaces on sciatic nerves and sciatic nerve branches, i.e., a common peroneal (CP) nerve in rats to activate tibialis anterior (TA) muscle.

2. System and device configuration, and working mechanism

Fig. 1e–i shows the schematic diagram of conceptual system using TENGs and neural interfaces for neuromodulation. The TENGs, driven by muscle movement from human body (Fig. 1e–f), generate electrical energy and transfer the energy to a CP nerve by neural interfaces (Fig. 1g–h) to activate the TA muscle (Fig. 1i). Direct stimulation of low frequency, generated by the muscle movement, may benefit simple and natural activation of targeted muscles more than stimulation by the other external sources that require additional components (coils and circuits etc.) and complicated procedures.

We deploy TENGs with multilayer stacked design to provide high current in experiments (Fig. 1f). The detailed fabrication process of the multilayer stacked TENG are described in the Supplementary material (Fig. S1a–c). For mechanical support, a PET sheet is used for zigzag-shaped structure. This structure can provide both the space for assembly of the multilayer stacked TENG and the recovery force when the press is released. After folding the PET into the zigzag shape, the Cu films are attached on two pairs of contact layers. PDMS layers with micro-pyramid patterns are assembled on the bottom Cu electrode for each pair of the layer. To optimize confinement height, PET films with different lengths are applied to encompass the stacked TENG device.

The neural interfaces are fabricated using microelectromechanical system (MEMS) technology. It consists of two layers of flexible polyimide with gold sandwiched in between in a sling-shape geometry. The detailed fabrication procedures are described in the Supplementary material (Fig. S1d–h).

The working mechanism of the TENG is depicted in Fig. S2. When the device is pressed, all layers contact with each other leading to triboelectric surface charge generation on the patterned PDMS and the top copper films (Fig. S2b). After the force is removed, the potential increment at the top electrode with respect to the bottom electrode leads to current flow from the top electrode to the bottom electrode while releasing the device (Fig. S2c). When the device is completely released, all the triboelectric layers reach in electrostatic equilibrium (Fig. S2d). The reduction of the potential at the two electrodes drives the current flows in the opposite direction when the stacked device is pressed again (Fig. S2e). After the second contact, one cycle of the power generation is completed and another cycle continues. The

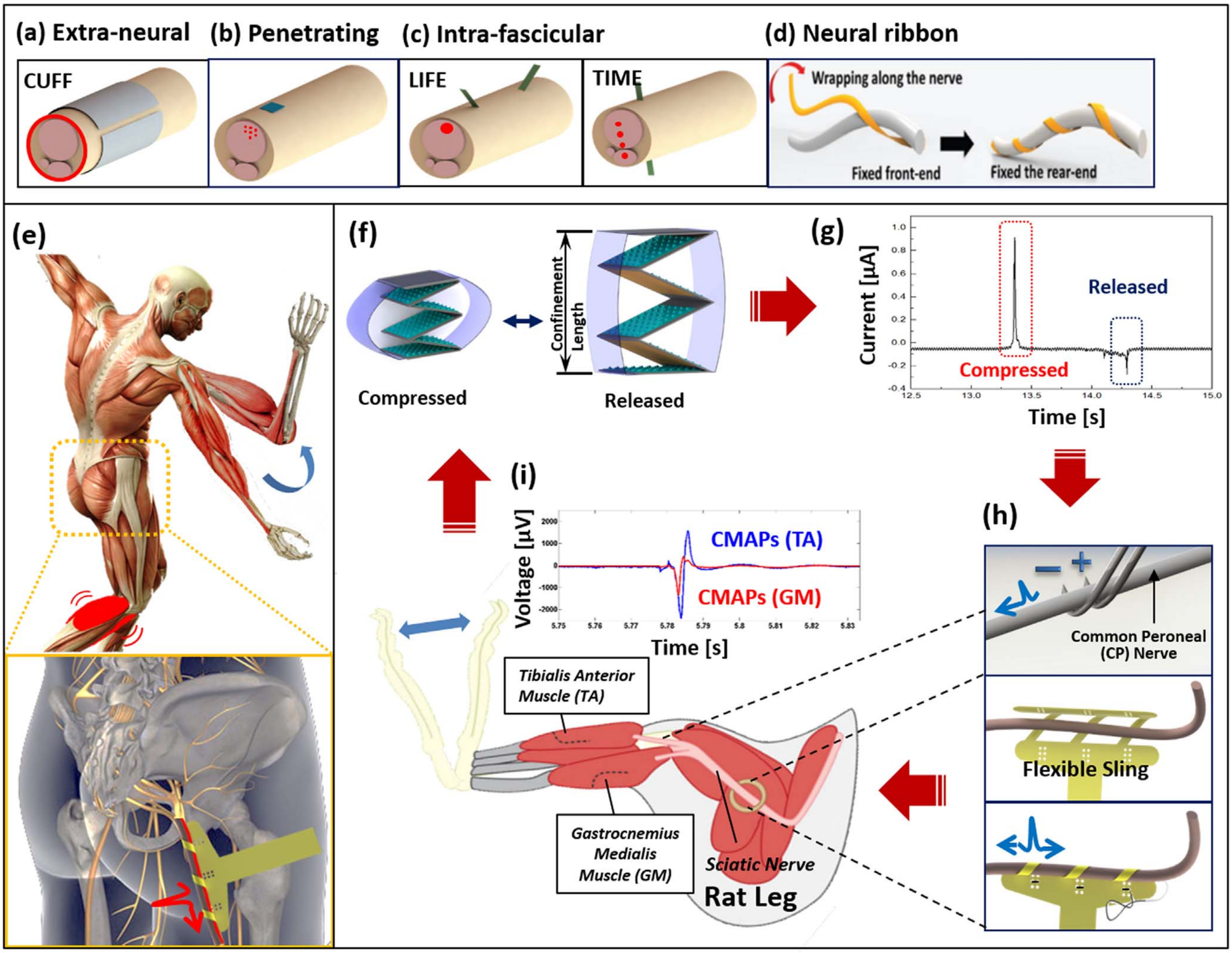

Fig. 1. Schematic diagram of the conceptual system using flexible neural interfaces and triboelectric nanogenerators (TENGs). Schematic diagram of (a) extra-neural, (b) penetrating, (c) intra-fascicular, and (d) flexible ribbon electrode [72]. (e) Schematic diagram of the conceptual system using a flexible sling interface and a TENG in human. (f) Schematic diagram of the TENG in a compressed state and a released state. (g) The generated current by the TENG. (h) Schematic diagram of the flexible and adjustable sling interface and (i) leg contraction with compound muscle action potential (CMAP) recordings of tibialis anterior (TA) and gastrocnemius medialis (GM) muscles.

detailed working mechanism of the TENGs can be found in the Supplementary material (Fig. S2).

3. In vitro characterization of triboelectric nanogenerators (TENGs)

To study the effect of the stacked multiple layers on overall device performance, various parameters, such as electrical connections, the number of stacked layers, the frequency of applied force and the confinement length, were studied. Thereafter, we demonstrated bio-mechanical energy harvesting using human hand and heel strike for practical applications.

An oscilloscope (DSOX3034 A, Agilent Technologies) with a probe (100 MΩ) was used to measure voltages of the device. For current measurements, low noise current preamplifier (SR570, Stanford Research Systems) was connected to the oscilloscope to measure the current in the form of voltage signal. The power characteristic measurement of the stacked TENGs was conducted by connecting load resistances in series across the device and measured the voltage across the resistor. The measured voltage was then used to calculate the power dissipation in the load resistor.

To demonstrate the configuration of electrical connection among the layers, we compared the output voltage and current of 5 stacked-layers connected in parallel and series, respectively. A probe with 100 MΩ load resistance was used for the voltage measurement. A detailed theoretical analysis can be found in the Supplementary material (Figs. S3 and S4).

The voltage output is shown in Fig. 2a and d for the parallel and the series configurations, respectively. The voltage (connected the probe of 100 MΩ load resistance) of the parallel configuration was 68 V, which is slightly lower than that of the series configuration which was 76 V. The estimated open circuit voltage for series connection was 192.2 V and for parallel connection was 76.8 V. The connection in series can provide much higher open circuit voltage than that of connection in parallel. However, the short circuit currents of the parallel configuration was 1.9 μA which is much higher than that of the series configuration, 0.8 μA, as shown in Fig. 2b and e. This result indicates that the parallel electrical connection is suitable for improving higher current output whereas the series connection in same polarity leads to increase in peak output voltage. It is noticeable that the voltage signals of the series configuration are asymmetric showing that the positive peaks are much higher than the negatives peaks. This phenomenon is induced by inner impedance change of the series configuration while separation process of the layers. The positive peaks are generated when the device is fully compressed while the negative peaks are generated when all the triboelectric pairs separate from each other. During this separation process, the total inner impedance immediately becomes very large once the first pair separates, which is very close to open

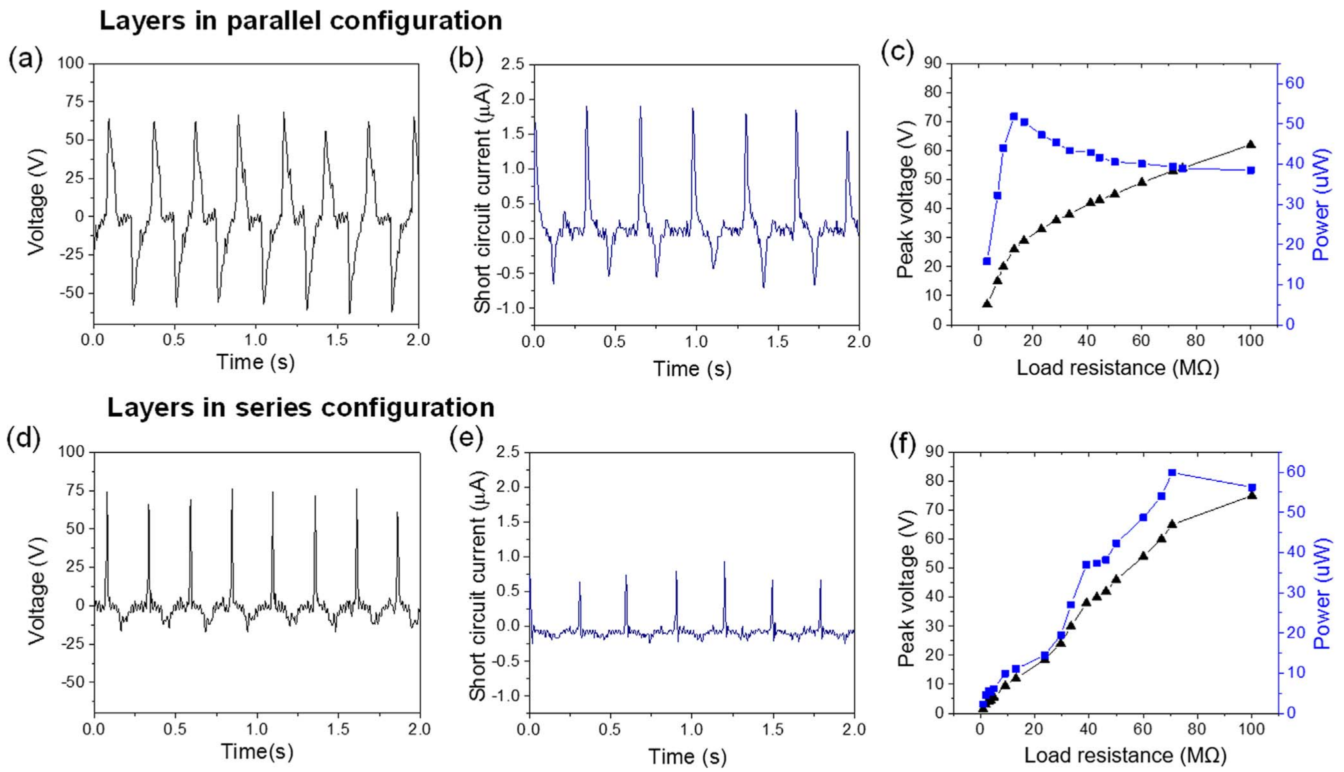

Fig. 2. Effect of electrical connections on stacked device with 5 layers. (a) Output voltage, (b) short circuit current, and (c) voltage and power characteristics for layers connected in parallel configuration; (d) output voltage (e) short circuit current and (f) voltage and power characteristics for layers connected in series configuration.

circuit. Then, the resistance of the probe become much smaller than the inner impedance and only a small portion of the voltage can be measured. That is why the negative peaks will be much smaller than the positive peaks. Whereas, for the parallel configuration, the total inner impedance of the device will not significantly increase until all the triboelectric pairs separate from each other. Thus the charge transfer process will not be affected greatly.

Thereafter, the voltage and power characteristics were measured depending on different values of load resistances. Fig. 2c and f show the power and voltage characteristics of the 5 layer stacked device. The peak power of the layers connected in the parallel was 51.8 μW at the load resistance of 15 MΩ (the 100 MΩ probe connect in parallel with measured load resistance of 13 MΩ). For the layers connected in the series configuration, the maximum power was 59.8 μW at the load resistance of 239 MΩ (the 100 MΩ probe connect in parallel measured load resistance of 70.5 MΩ). Even though the maximum powers of the two configurations show the similar level, the decrement of the maximum power in series configuration is significant when the load resistance value is reduced. It demonstrates that the parallel configuration is suitable for neural stimulation since the impedance between a sensing electrode of neural interfaces and a sciatic nerve is typically degree of kΩ. We used the parallel configuration for the rest of characterizations.

We demonstrated the effect of the number of layer, frequency, and confinement length to optimize the performance of the device. Firstly, we increased the number of stacked layers at a fixed frequency of 4 Hz and a fixed confinement of 4 cm to demonstrate corresponding change in the output voltage and short circuit current. The peak output voltage remains almost constant (Fig. 3a) whereas the short circuit current increases linearly from 0.3μA to 1.7 μA as the number of the layers increase from 1 to 5 (Fig. 3b), respectively. Then the 5 layered multi-stacked device was tested at different frequency of the applied force at a confinement distance of 4 cm as shown in Fig. 3c and d. Both the voltage and the current increase proportional to the frequency, which can be explained by the increased impact force as the frequency of applied force increases [81]. As for the equal level of force, the surface charge generated is same, the decrease in time interval between repeated impacts leads to higher output voltage and current. Detailed signal samples can be found in the Supplementary material (Fig. S5). Since a larger separation distance results in higher triboelectric output, only characterizing the relation between the confinement length and triboelectric output is not very meaningful. Here we made a comparison between devices with 5 stacked layer and 15 stacked layer in the same condition to know how to achieve higher output with a fixed volume. The output voltage and current of 5 stacked layer and 15 stacked layer devices are shown in Fig. 3e and g, respectively. It was observed that for smaller values of confinement lengths, both the peak output voltage and short circuit current increased but started saturating after a confinement length value of 3 cm for 5-layer device and 4 cm for 15-layer device, respectively. Compared with the 15-layer device, the 5-layer device had a slightly higher output voltage but a much lower current. The higher voltage of the 5-layer device can be attributed to the larger spacer assigned to each triboelectric pair when the total confinement length is the same for both the 5-layer device and the 15-layer device. Because the total output voltage is mainly determined by the output of an individual layer that is affected by the separation length. Then, we fixed the confinement length of 4 mm and force frequency of 2 Hz for both device and characterized the maximum output power and inner impedance. As can be seen in Fig. 3f and h, because of the parallel configuration, compared with the 5-layer device, the 15-layer device can provide a higher output power and much lower inner impedance while the output voltage at 100 MΩ load keeps also constant, which is in accordance with the theoretical model discussed in the Supplementary material (Figs. S3 and S4). All the detailed signal sample of characterization can be found in the Supplementary material (Fig. S5). A practical demonstration of energy harvesting using the 5-layer device by hand clapping and heel strike can be found in the Supplementary material (Fig. S6).

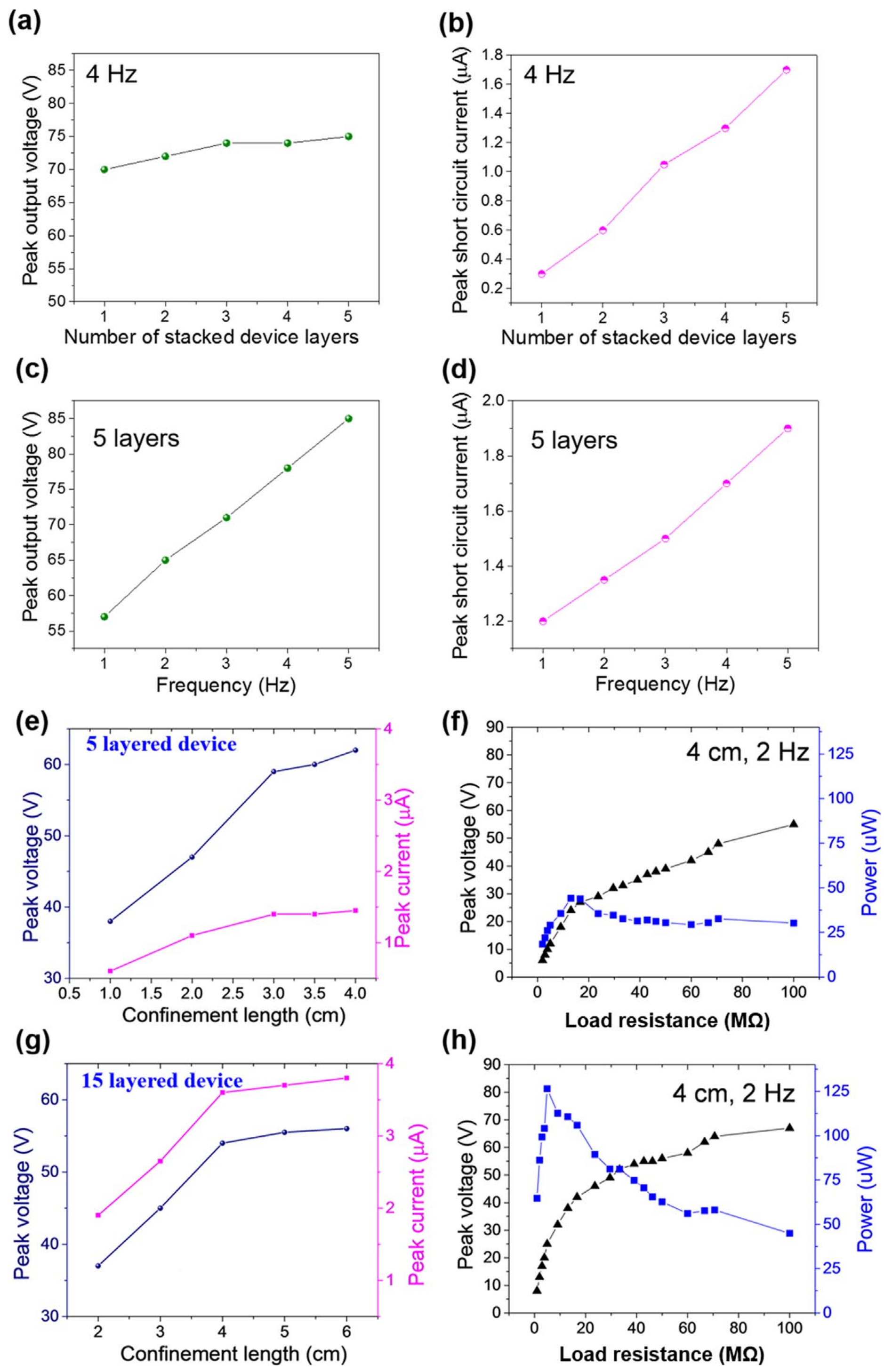

Fig. 3. (a) Peak output voltage (measured with a 100 MΩ probe) for different device layers at 4 Hz; (b) peak short circuit current for different device layers at 4 Hz; (c) peak output voltage (measured with a 100 MΩ probe) for different frequencies for 5 layered device; (d) peak short circuit current for different frequencies for 5 layered device; (e) variation of peak voltage and short circuit current with different confinement lengths for 5 layered device; (f) output voltage and power with different load resistance for 5 layered device with 4 cm confinement length at 2 Hz; (g) variation of peak voltage and short circuit current with different confinement lengths for 15 layered device; (h) output voltage and power with different load resistance for 15 layered device with 4 cm confinement length at 2 Hz.

4. Selective recording and stimulation using flexible neural interface

4.1. Device design

The flexible and adjustable sling electrodes have six active electrodes (each 100 μm diameter) on a central bridge and two ring electrodes that surround the nerve on two neighboring bridges (Fig. 4a). The three bridges are angled so that it allows the active electrodes to be helically implanted around a nerve while keeping a distance of 3 mm between the rings and the active electrodes (yellow arrows in Fig. 4a). This enables the electrode to reduce the pressure applied on the nerve surface while making good contact. Also, it allows a mixed tripole, where two rings acting as reference electrodes are shorted together, to perform better than other recording configurations in terms of high SNR [82]. In addition, this design allows us to set transverse or

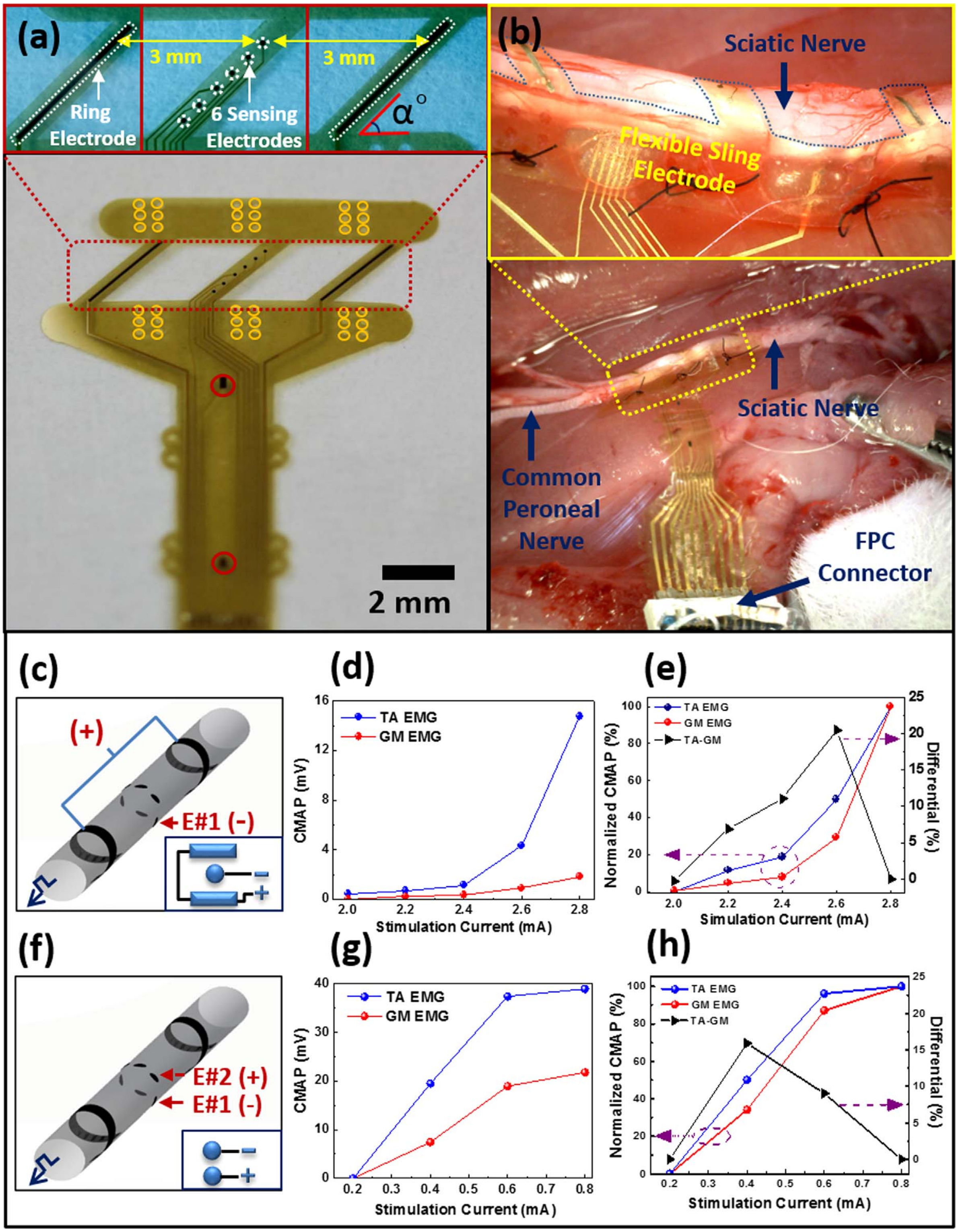

Fig. 4. (a) Picture of a fabricated sling electrode and (b) picture of the implanted flexible sling electrode on a rat sciatic nerve. The results of selective stimulation on rat sciatic nerves depending on different configuration. (c) Schematic diagram of the longitudinal tripolar configuration, (d) compound muscle action potentials (CMAPs), and (e) normalized CMAP with corresponding to selectivity depending on stimulation currents. (f) Schematic diagram of the transverse configuration, (g) CMAP, and (h) normalized CMAP with corresponding to selectivity depending on stimulation currents.

longitudinal tripolar configurations for selective stimulation. Fig. 1h (bottom) shows how the sling electrodes were implanted on the sciatic nerve, in a manner analogous to hanging a nerve in a sling. Furthermore, several suturing holes on the body of the electrode (yellow circles in Fig. 4a) enable surgeons to suture the appropriate holes together with surgical thread to fit various sizes of nerves (diameter: 0.7–1.2 mm). Thus, it can easily be used on nerves with slightly different sizes. In contrast, for cuff-type electrodes, the inner diameter of a nerve cuff has to be closely matched to the size of the nerve, so different cuff electrodes have to be prepared for nerves with slightly different sizes.

To enhance the performance of the electrochemical interface, the fabricated electrodes were subsequently coated with platinum (Pt) black, which has been commonly used for neural recording and stimulation [83–85]. The detailed electrochemical characterization is also described in the Supplementary material (Fig. S7). The prepared Pt-coated electrodes were then implanted on sciatic nerves in rats for *in vivo* tests (Note 1 in the Supplementary material).

4.2. Neural recording of evoked CNAPs on sciatic nerves

For selective recording experiments, compound neural action potentials (CNAPs) from the main sciatic nerve were partially evoked by stimulating the CP nerve branch of the sciatic nerve (Fig. 1h, top). The evoked CNAPs were, then, individually recorded through the six active contacts (Fig. S8). Fig. S8c shows the mean and standard error (n=50) of the latency of the peaks from each of the six electrodes when stimulated with a current amplitude of 1.2 mA. The latency of the peak of the CNAP is important since it provides an estimation of the nerve conduction velocity (NCV). The mean latency for E#1 was 0.26 ms, while that for E#6 was 0.3 ms. This indicates that the six sensing electrodes made good contact with the nerve since the contacts were positioned helically around the main trunk where E#1 was closer to the stimulation site while E#6 was further away from the stimulation site. Since the distance between two electrodes (E#1 and #6) was 1.3 mm, NCV was 32.5 m s^{-1} (Note 2 in the Supplementary material). Also, the NCV matches well with the established NCV of the fastest fibers in rat sciatic nerve from literature [86–88]. Fig. S8d illustrates the mean and standard error (n=50) of the recorded amplitudes on different electrode contracts under stimulation currents of 1.2 mA. The recorded amplitudes on E#1 were the largest, while those of E#4 were the lowest. The results indicate that the location of the CP nerve inside the sciatic nerve was closer to E#1 than E#4. The maximum difference between E#1 and E#4 was 48% when stimulated with 0.4 mA. The difference decreased with increasing current amplitudes until 32% with 1.2 mA. The difference did not change beyond that. This may be due to the fact that the larger stimulation current amplitudes fully activated all the nerve fibers in the CP nerve. Our results demonstrated that all six recording electrodes positioned around the nerve were able to record CNAPs successfully.

4.3. Selective stimulation on sciatic nerves

To investigate the ability of the sling electrodes to perform selective stimulation, we positioned the sling electrode around the sciatic nerve while recording compound muscle action potentials (CMAPs) from the gastrocnemius medialis (GM) and tibialis anterior (TA) muscles. As shown in Fig. S9a, the difference in the activation of TA-GM on E#1 was 20.5% at 2.6 mA, indicating that the TA muscle was stimulated more than the GM muscle under this condition. The difference on E#3 was negligible, meaning that the GM and TM muscles were activated together across the different stimulation intensities (Fig. S9b). The difference on E#5 was −14.3 to −16.9% when stimulated with current amplitudes in the range of 2.2–2.4 mA, demonstrating that the GM muscle was stimulated more than the TA muscles under this condition (Fig. S9c). The results demonstrate that the TA muscle can be activated more strongly through E#1 than E#3 or #E5. This matches up with the recording results discussed earlier in that stimulation of the CP nerve (which controls the TA muscle [77]) resulted in the largest amplitudes on E#1. Thus, it is not surprising that stimulation on E#1 resulted in larger activation of the TA muscle.

We also explored stimulation using the transverse configuration in order to compare with the longitudinal tripolar configuration for the sling electrodes. E#1 and E#2 were selected for the transverse stimulation since E#1 showed the highest selectivity (Fig. 4c–h). The CMAPs measured from the GM and TA muscles are plotted against stimulation current amplitudes in Fig. 4d and g. In addition, the normalized CMAPs from the GM and TA muscles, as well as the difference between the normalized CMAPs, are plotted against the stimulation current amplitudes in Fig. 4e and h. One significant difference between the two configurations was the stimulation current required to activate the muscles. As shown in Fig. 4d and g, the longitudinal tripolar configuration activated the muscles from 2.4 mA, while the transverse stimulation activated the muscles from 0.4 mA. Higher current amplitudes normally carry the risk of nerve damage and delamination of electrodes. In addition, the transverse stimulation activated CMAPs with a higher amplitude than that of the longitudinal stimulation, which suggests that it may be able to generate more effective stimulation of the muscles. A previous study using multipolar cuff electrodes also showed similar results [89].

4.4. Hemodynamic measurement by functional photoacoustic microscopy (fPAM)

To verify whether the sling electrodes affect the hemodynamics of the sciatic nerve, we used functional photoacoustic microscopy (fPAM) to image the blood flow through the blood vessels on the nerve surface before and after implantation of the sling electrodes. We also imaged the blood flow after the implantation of a commercial cuff electrode (Microprobe Inc., Gaithersburg, MD, USA) (inner diameter: 0.75 mm). These results are shown in the images in Fig. 5. The yellow arrows in the left panels indicate the blood vessel cross-sectional direction of the photoacoustic (PA) B-scan images. Laser pulses at a visible wavelength of 570 nm (λ_{570}) was employed for the PA wave excitation. These wavelengths were used because the detected PA signals at λ_{570} were dominated by changes in cerebral blood volume (CBV) and this reveals crucial information about the nerve hemodynamics [90]. The blood vessels were also identified in the PA B-scan image at λ_{570}, and all PA images and values were normalized to the maximum change in the $I_{R(570)}$ image. There was a significant reduction in the CBV (i.e., R_{CBV}) following cuff implantation (Fig. 5a–d). However, there were no significant changes in the CBV values before and after sling implantation (Fig. 5e–h). This indicates that the sling electrodes did not cause any changes in the blood flow in the nerve, while cuff electrodes can significantly exert changes in nerve hemodynamics.

5. In vivo test of triboelectric nanogenerator and neural interface

To demonstrate a battery-free neural interface, we conducted selective stimulation to activate the TA muscle using the sling interface connected with the TENG. The sling interface was implanted on the sciatic nerve and two active electrodes were selected for the transverse configuration which enabled to activate the TA muscle more than the GM muscle. The TENG was then connected to the two electrodes of the sling interface (Fig. 6a). The TENG was fully tapped by a hand to activate the TA muscle. The record of the stimulation is shown Video S1 in the Supporting information file. In Fig. 6b, the recorded CMAPs of GM (red) and TA (blue) muscles show that the TA muscle was activated more effectively than the GA muscle. We observed the twitch of the muscle, however, the muscle contraction was not strong enough for the ankle dorsiflexion. This may be due to fact that the charge was higher than the threshold of the muscle activation, but was not enough for the completed contraction of the TA muscle.

Supplementary material related to this article can be found online at http://dx.doi.org/10.1016/j.nanoen.2016.12.038.

To fully demonstrate modulation of the TA muscle, we connected the TENG to a pair of Pt/Ir wires, i.e., stimulation electrode, and implanted on the CP nerve (Fig. 6c). The TENG was tapped by a hand with different frequencies while the CMAPs of GM and TA muscles were recorded. As expected, the TA muscle was activated more than the GA muscle while stimulating the CP nerve. It is not surprising that a CP nerve innervates TA muscle more than GM as we discussed above. We observed the muscle twitch and contraction and it became strong when

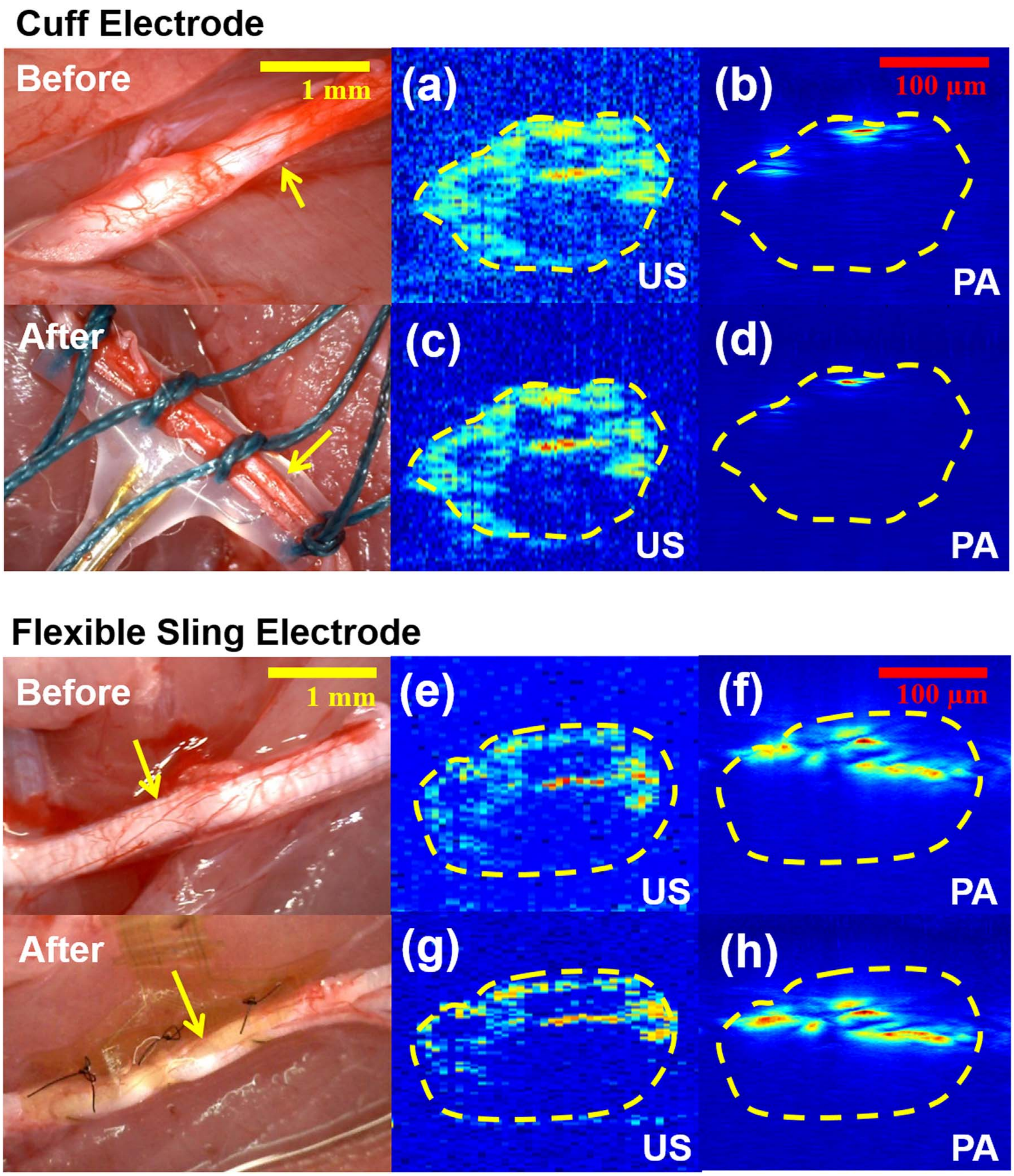

Fig. 5. Picture of sciatic nerves before and after implantation of a commercial cuff and the sling electrode, respectively (left). The results of functional photoacoustic measurements (right). (a) US image of the targeted blood vessel and (b) *in vivo* $I_{R(570)}$ PA B-scan image reflected the blood volume changes before implantation. (c) US image and (d) *in vivo* $I_{R(570)}$ PA B-scan image of the same position after the implantation of the cuff electrode. (e) US image and (f) *in vivo* $I_{R(570)}$ PA B-scan image before implantation. (g) US image and (h) *in vivo* $I_{R(570)}$ PA B-scan image after the implantation of the sling electrode.

we tapped with higher frequency on the device. The record of the stimulation is shown Video S2 in the Supporting information file. The activation via the CP nerve was more effective than the activation via the sciatic nerve by the sling electrode. This is because that approaching small nerves enhances the selectivity. We tracked the recorded CMAPs depending on frequencies to verify our observation. Fig. 6d shows current peaks generated by the TENG and Fig. 6e shows the EMG recording at 2 Hz. The amplitude of CMAPs from the TA muscle was 1932.6 μV and that from the GM muscles of 834.5 μV. Fig. 6f and g show current peaks generated by the TENG and the EMG recording, respectively, at 4 Hz. The amplitude of CMAPs from the TA muscle was 6164 μV and that from the GM muscles of was 1720.3 μV. This is because, by using the hand tapping approach, the actual impact force on the TENG increases as the tapping frequency due to the nature of human hand behavior. The increased impact force associated with higher tapping frequency leads to higher output voltage. Thereby the muscles are activated more in this case. It demonstrates that the TENG is able to generate enough charge to control a TA muscle though a direct common peroneal nerve stimulation.

Supplementary material related to this article can be found online at http://dx.doi.org/10.1016/j.nanoen.2016.12.038.

6. Concluding remarks

We developed a flexible and adjustable neural interface as a generic electrode for selective stimulation and recording for a sciatic nerve. The

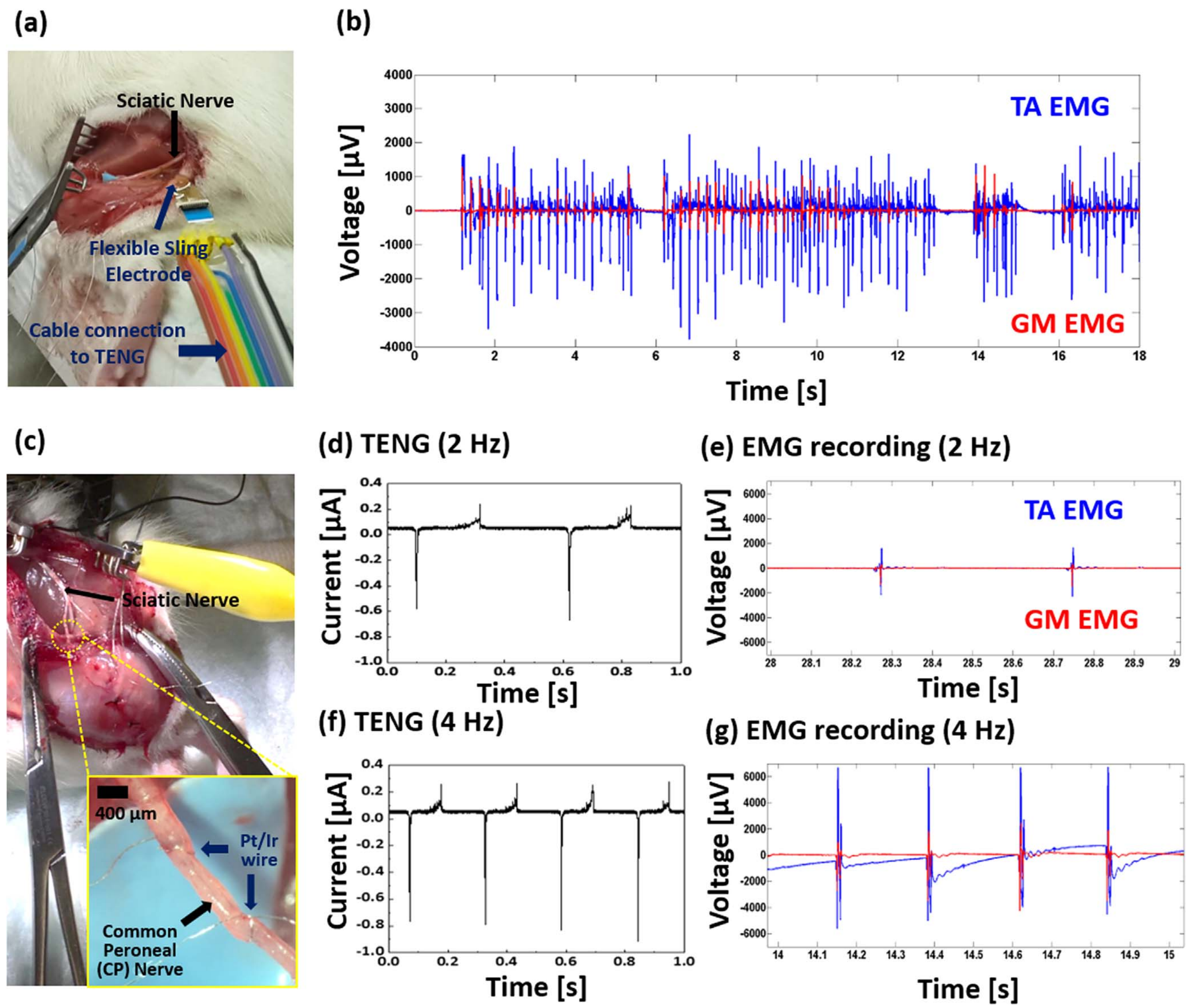

Fig. 6. (a) Picture of *in vivo* direct stimulation test using the sling interface and the TENG as direct stimulation source. (b) The recorded compound muscle action potentials (CMAPs) of GM (red) and TA (blue) muscles by the battery-free sling interface. (c) Picture of *in vivo* direct TENG stimulation test using a pair of Pt/Ir wires on common peroneal (CP) nerve (inset). (d) Current peaks generated by the TENG and (e) the CMAPs recordings at 2 Hz. (f) Current peaks generated by the TENG and (g) the CMAPs recordings at 4 Hz.

results of the selective recording demonstrated that compound neural action potentials (CNAPs) were clearly recorded with different amplitudes and latencies. It indicated the location of the particular axon inside the sciatic nerve connecting to a common peroneal (CP) nerve, i.e., a small branch of sciatic nerve, and provided a reasonable nerve conduction velocity (NCV) of the sciatic nerve. In addition, the results of the selective stimulation demonstrated that different muscle activation patterns of gastrocnemius medialis (GM) and tibialis anterior (TA) muscles were achieved. It also suggested that transverse configuration can provide more effective stimulation of the muscles. For the validation test of the sling interface for the pressure applied on the nerve, we demonstrated the blood flow measurement demonstrating that the pressure applied on the nerve by the flexible neural interface was less than that applied by commercial cuff electrodes.

We also demonstrated stacked TENGs with confinement that provided clear optimization range. It allowed us to tap fingers for reliable TENG energy harvesting outside body and may have benefit of implantation inside body in the future.

To achieve battery-free neutral electrodes, the sling interface connected with the triboelectric nanogenerators (TENGs) was implanted on a sciatic nerve to selectively activate the TA muscle. Furthermore, we demonstrated stimulation of the CP nerve using the TENGs combined with a pair of Pt/Ir wires to control a TA muscle. The degree of activation of the muscle was controlled by the operation of the device. Overall results demonstrate that we achieved direct stimulation of a sciatic nerve and a branch nerve in alive animals using the TENGs connected with neural interfaces. With these facts, the flexible TENG integrated with neural interface can achieve a battery-free wearable neuromodulator. Furthermore, based on the previous study of implantable TENGs with biocompatible encapsulation [46], integration of such implantable TENGs with our neural interfaces may result in implantable and battery-free neuromodulator in the future.

Acknowledgements

The authors acknowledge the financial support from following research grants: NRF-CRP8-2011-01 Program ‘Self-powered body sensor for disease management and prevention-orientated healthcare’ (R-263-000-A27-281), and NRF-CRP10-2012-01 Program ‘Peripheral Nerve Prostheses: A Paradigm Shift in Restoring Dexterous Limb Function’ (R-719-000-001–281) from the National Research

Foundation (NRF), Singapore and Faculty Research Committee (FRC) grant (R-263-000-B56-112) "Thermoelectric Power Generator (TEG) Based Self-Powered ECG Plaster – System Integration (Part 3)" at the National University of Singapore.

Appendix A. Supplementary material

Supplementary data associated with this article can be found in the online version at doi:10.1016/j.nanoen.2016.12.038.

References

[1] K. Famm, B. Litt, K.J. Tracey, E.S. Boyden, M. Slaoui, Nature 496 (2013) 159–161.
[2] S. Reardon, Nature 511 (2014) 18.
[3] A.P. Amar, M.L. Levy, C.Y. Liu, M.L.J. Apuzzo, Proc. IEEE 96 (2008) 1142–1151.
[4] X. Wang, L. Dong, H. Zhang, R. Yu, C. Pan, Z.L. Wang, Adv. Sci. 2 (2015) 1500169.
[5] R. Hinchet, W. Seung, S.W. Kim, ChemSusChem 8 (2015) 2327–2344.
[6] F.R. Fan, W. Tang, Z.L. Wang, Adv. Mater. 28 (2016) 4283–4305.
[7] H. Wang, G. Pastorin, C. Lee, Adv. Sci. (Weinh.) 3 (2016) 1500441.
[8] H. Wang, Z. Xiang, P. Giorgia, X. Mu, Y. Yang, Z.L. Wang, C. Lee, Nano Energy 23 (2016) 80–88.
[9] T.Q. Trung, N.E. Lee, Adv. Mater. 28 (2016) 4338–4372.
[10] Y. Khan, A.E. Ostfeld, C.M. Lochner, A. Pierre, A.C. Arias, Adv. Mater. 28 (2016) 4373–4395.
[11] S. Choi, H. Lee, R. Ghaffari, T. Hyeon, D.H. Kim, Adv. Mater. 28 (2016) 4203–4218.
[12] S. Kim, J.S. Ho, L.Y. Chen, A.S.Y. Poon, Appl. Phys. Lett. 101 (2012) 073701.
[13] R. Jegadeesan, S. Nag, K. Agarwal, N.V. Thakor, Y.X. Guo, IEEE J. Biomed. Health Inform. 19 (2015) 958–970.
[14] J.S. Ho, A.J. Yeh, E. Neofytou, S. Kim, Y. Tanabe, B. Patlolla, R.E. Beygui, A.S. Poon, Proc. Natl. Acad. Sci. USA 111 (2014) 7974–7979.
[15] R. Latham, Solid State Ion. 172 (2004) 7–11.
[16] D.C. Bock, A.C. Marschilok, K.J. Takeuchi, E.S. Takeuchi, Electrochim. Acta 84 (2012).
[17] J. Xie, C. Lee, H. Feng, J. Microelectromech. Syst. 19 (2010) 317–324.
[18] J.H. We, S.J. Kim, B.J. Cho, Energy 73 (2014) 506–512.
[19] Z. Lu, H. Zhang, C. Mao, C.M. Li, Appl. Energy 164 (2016) 57–63.
[20] S.J. Kim, J.H. We, B.J. Cho, Energy Environ. Sci. 7 (2014) 1959.
[21] M. Hyland, H. Hunter, J. Liu, E. Veety, D. Vashaee, Appl. Energy 182 (2016) 518–524.
[22] H. Zhang, X.S. Zhang, X. Cheng, Y. Liu, M. Han, X. Xue, S. Wang, F. Yang, S.A. Shankaregowda, H. Zhang, Z. Xu, Nano Energy 12 (2015) 296–304.
[23] X. Cheng, X. Xue, Y. Ma, M. Han, W. Zhang, Z. Xu, H. Zhang, H. Zhang, Nano Energy 22 (2016) 453–460.
[24] G.T. Hwang, Y. Kim, J.H. Lee, S. Oh, C.K. Jeong, D.Y. Park, J. Ryu, H. Kwon, S.G. Lee, B. Joung, D. Kim, K.J. Lee, Energy Environ. Sci. 8 (2015) 2677–2684.
[25] C.K. Jeong, S.B. Cho, J.H. Han, D.Y. Park, S. Yang, K.I. Park, J. Ryu, H. Sohn, Y.C. Chung, K.J. Lee, Nano Res. (2016).
[26] G. Sahara, W. Hijikata, K. Tomioka, T. Shinshi, Proc. Inst. Mech. Eng. H 230 (2016) 569–578.
[27] F.-R. Fan, Z.-Q. Tian, Z.L. Wang, Nano Energy 1 (2012) 328–334.
[28] G. Zhu, Z.-H. Lin, Q. Jing, P. Bai, C. Pan, Y. Yang, Y. Zhou, Z.L. Wang, Nano letters 13 (2013) 847–853.
[29] Y. Xie, S. Wang, L. Lin, Q. Jing, Z.-H. Lin, S. Niu, Z. Wu, Z.L. Wang, ACS Nano 7 (2013) 7119–7125.
[30] B. Meng, W. Tang, Z.-h Too, X. Zhang, M. Han, W. Liu, H. Zhang, Energy Environ. Sci. 6 (2013) 3235–3240.
[31] L. Dhakar, P. Pitchappa, F. Tay, C. Lee, Nano Energy (2015).
[32] J. Chen, G. Zhu, W. Yang, Q. Jing, P. Bai, Y. Yang, T.C. Hou, Z.L. Wang, Adv. Mater. 25 (2013) 6094–6099.
[33] G. Zhu, J. Chen, T. Zhang, Q. Jing, Z.L. Wang, Nat. Commun. 5 (2014).
[34] Z.H. Lin, G. Cheng, L. Lin, S. Lee, Z.L. Wang, Angew. Chem. Int. Ed. 52 (2013) 12545–12549.
[35] Y. Yang, H. Zhang, Z.L. Wang, Adv. Funct. Mater. 24 (2014) 3745–3750.
[36] R. Hinchet, S.W. Kim, ACS Nano 9 (2015) 7742–7745.
[37] J. Chun, B.U. Ye, J.W. Lee, D. Choi, C.Y. Kang, S.W. Kim, Z.L. Wang, J.M. Baik, Nat. Commun. 7 (2016) 12985.
[38] X.H. Li, C.B. Han, L.M. Zhang, Z.L. Wang, Nano Res. 8 (2015) 3197–3204.
[39] R.G. Horn, D.T. Smith, Science 256 (1992) 362–364.
[40] H. Baytekin, A. Patashinski, M. Branicki, B. Baytekin, S. Soh, B.A. Grzybowski, Science 333 (2011) 308–312.
[41] J. Lowell, A. Rose-Innes, Adv. Phys. 29 (1980) 947–1023.
[42] J. Sun, W. Li, G. Liu, W. Li, M. Chen, J. Phys. Chem. C 119 (2015) 9061–9068.
[43] K.N. Kim, J. Chun, S.A. Chae, C.W. Ahn, I.W. Kim, S.W. Kim, Z.L. Wang, J.M. Baik, Nano Energy 14 (2015) 87–94.
[44] F.R. Fan, Z.Q. Tian, Z.L. Wang, Nano Energy 1 (2012) 328–334.
[45] B. Meng, W. Tang, X.S. Zhang, M. Han, W. Liu, H. Zhang, Nano Energy 2 (2013) 1101–1106.
[46] P. Bai, G. Zhu, Z.H. Lin, Q. Jing, J. Chen, G. Zhang, J. Ma, Z.L. Wang, ACS Nano 7 (2013) 3713–3719.
[47] Q. Zheng, H. Zhang, B. Shi, X. Xue, Z. Liu, Y. Jin, Y. Ma, Y. Zou, X. Wang, Z. An, W. Tang, W. Zhang, F. Yang, Y. Liu, X. Lang, Z. Xu, Z. Li, Z.L. Wang, ACS Nano 10 (2016) 6510–6518.
[48] Q. Zheng, B. Shi, F. Fan, X. Wang, L. Yan, W. Yuan, S. Wang, H. Liu, Z. Li, Z.L. Wang, Adv. Mater. 26 (2014) 5851–5856.
[49] Y. Ma, Q. Zheng, Y. Liu, B. Shi, X. Xue, W. Ji, Z. Liu, Y. Jin, Y. Zou, Z. An, W. Zhang, X. Wang, W. Jiang, Z. Xu, Z.L. Wang, Z. Li, H. Zhang, Nano Lett. 16 (2016) 6042–6051.
[50] Z. Li, G. Zhu, R. Yang, A.C. Wang, Z.L. Wang, Adv. Mater. 22 (2010) 2534–2537.
[51] Q. Zheng, Y. Zou, Y. Zhang, Z. Liu, B. Shi, X. Wang, Y. Jin, H. Ouyang, Z. Li, Z.L. Wang, Sci. Adv. 2 (2016) e1501478.
[52] X.S. Zhang, M.D. Han, R.X. Wang, B. Meng, F.Y. Zhu, X.M. Sun, W. Hu, W. Wang, Z.H. Li, H.X. Zhang, Nano Energy 4 (2014) 123–131.
[53] N. Yogeswaran, W. Dang, W.T. Navaraj, D. Shakthivel, S. Khan, E.O. Polat, S. Gupta, H. Heidari, M. Kaboli, L. Lorenzelli, G. Cheng, R. Dahiya, Adv. Robot. 29 (2015) 1359–1373.
[54] Y. Diao, B.C. Tee, G. Giri, J. Xu, D.H. Kim, H.A. Becerril, R.M. Stoltenberg, T.H. Lee, G. Xue, S.C. Mannsfeld, Z. Bao, Nat. Mater. 12 (2013) 665–671.
[55] L.Y. Chen, B.C. Tee, A.L. Chortos, G. Schwartz, V. Tse, D.J. Lipomi, H.S. Wong, M.V. McConnell, Z. Bao, Nat. Commun. 5 (2014) 5028.
[56] B.C. Tee, C. Wang, R. Allen, Z. Bao, Nat. Nanotechnol. 7 (2012) 825–832.
[57] B.C.K. Tee, A. Chortos, A. Berndt, A.K. Nguyen, A. Tom, A. McGuire, Z.C. Lin, K. Tien, W.G. Bae, H. Wang, P. Mei, H.H. Chou, B. Cui, K. Deisseroth, T.N. Ng, Z. Bao, Science 350 (2015) 313–316.
[58] M.L. Hammock, A. Chortos, B.C. Tee, J.B. Tok, Z. Bao, Adv. Mater. 25 (2013) 5997–6038.
[59] A. Chortos, J. Liu, Z. Bao, Nat. Mater. 15 (2016) 937–950.
[60] M. Amjadi, K.-U. Kyung, I. Park, M. Sitti, Adv. Funct. Mater. 26 (2016) 1678–1698.
[61] J. Viventi, D.H. Kim, L. Vigeland, E.S. Frechette, J.A. Blanco, Y.S. Kim, A.E. Avrin, V.R. Tiruvadi, S.W. Hwang, A.C. Vanleer, D.F. Wulsin, K. Davis, C.E. Gelber, L. Palmer, J. Van der Spiegel, J. Wu, J. Xiao, Y. Huang, D. Contreras, J.A. Rogers, B. Litt, Nat. Neurosci. 14 (2011) 1599–1605.
[62] A.H. Park, S.H. Lee, C. Lee, J. Kim, H.E. Lee, S.B. Paik, K.J. Lee, D. Kim, ACS Nano 10 (2016) 2791–2802.
[63] D.J. Tyler, D.M. Durand, IEEE Trans. Neural Syst. Rehabil. Eng. 10 (2002) 294–303.
[64] J.K. Chapin, K.A. Moxon, Neural Prostheses for Restoration of Sensory and Motor Function, CRC Press LLC, USA, 2001.
[65] G.G. Naples, J.T. Mortimer, A. Scheiner, J.D. Sweeney, IEEE Trans. Biomed. Eng. 35 (1988) 905.
[66] D.W. Tan, M.A. Schiefer, M.W. Keith, J.R. Anderson, J. Tyler, D.J. Tyler, Sci. Transl. Med. 6 (2014) 257ra138.
[67] H.A. Wark, R. Sharma, K.S. Mathews, E. Fernandez, J. Yoo, B. Christensen, P. Tresco, L. Rieth, F. Solzbacher, R.A. Normann, P. Tathireddy, J. Neural Eng. 10 (2013) 045003.
[68] M.B. Christensen, S.M. Pearce, N.M. Ledbetter, D.J. Warren, G.A. Clark, P.A. Tresco, Acta Biomater. 10 (2014) 4650–4660.
[69] H.A. Wark, K.S. Mathews, R.A. Normann, E. Fernandez, J. Neural Eng. 11 (2014) 046027.
[70] N. Lago, K. Yoshida, K.P. Koch, X. Navarro, IEEE Trans. Biomed. Eng. 54 (2007) 281–290.
[71] T. Boretius, J. Badia, A. Pascual-Font, M. Schuettler, X. Navarro, K. Yoshida, T. Stieglitz, Biosens. Bioelectron. 26 (2010) 62–69.
[72] J. Badia, T. Boretius, A. Pascual-Font, E. Udina, T. Stieglitz, X. Navarro, IEEE Trans. Biomed. Eng. 58 (2011).
[73] S.P. Lacour, R. Atta, J.J. FitzGerald, M. Blamire, E. Tarte, J. Fawcett, Sens. Actuators A: Phys. 147 (2008) 456–463.
[74] S.P. Lacour, J.J. Fitzgerald, N. Lago, E. Tarte, S. McMahon, J. Fawcett, IEEE Trans. Neural Syst. Rehabil. Eng. 17 (2009) 454–460.
[75] I.P. Clements, V.J. Mukhatyar, A. Srinivasan, J.T. Bentley, D.S. Andreasen, R.V. Bellamkonda, IEEE Trans. Neural Syst. Rehabil. Eng. 21 (2013) 554–566.
[76] J. Scheib, A. Hoke, Nat. Rev. Neurol. 9 (2013) 668–676.
[77] M.A. Schiefer, M. Freeberg, G.J. Pinault, J. Anderson, H. Hoyen, D.J. Tyler, R.J. Triolo, J. Neural Eng. 10 (2013) 056006.
[78] Z. Xiang, S. Sheshadri, S.H. Lee, J. Wang, N. Xue, N.V. Thakor, S.C. Yen, C. Lee, Adv. Sci. 3 (2016) 1500386.
[79] Z. Xiang, S.C. Yen, S. Sheshadri, J. Wang, S. Lee, Y.H. Liu, L.D. Liao, N.V. Thakor, C. Lee, Adv. Mater. 28 (2016) 4472–4479.
[80] J.H. Burridge, D.L. McLellan, J. Neurol. Neurosurg. Psychiatry 69 (2000) 353–361.
[81] W. Tang, B. Meng, H. Zhang, Nano Energy 2 (2013) 1164–1171.
[82] M. Ortiz-Catalan, J. Marin-Millan, J. Delbeke, B. Hakansson, R. Branemark, J. Neuroeng. Rehabil. 10 (2013) 1–15.
[83] T. Boretius, T. Jurzinsky, C. Koehler, S. Kerzenmacher, H. Hillebrecht, T. Stieglitz, IEEE EMBS (2011) 5404–5407.
[84] Y.F. Rui, J.Q. Liu, B. Yang, K.Y. Li, C.S. Yang, Biomed. Microdevices 14 (2012) 367–373.
[85] C. Zhang, J.Q. Liu, H.C. Tian, X.Y. Kang, J.C. Du, Y.F. Rui, B. Yang, C.S. Yang, Microsyst. Technol. 21 (2013) 139–145.
[86] R.S. Martins, M.G. Siqueira, C.F.D. Silva, B.O.D. Godoy, J.P.P. Plese, Arq. Neuropsiquiatr. 63 (2005) 601–604.
[87] M.E. Walsh, L.B. Sloane, K.E. Fischer, S.N. Austad, A. Richardson, H. Van Remmen, J. Gerontol. A Biol. Sci. Med. Sci. 70 (2015) 1312–1319.
[88] S. Lee, S.C. Yen, S. Sheshadri, I. Delgado-Martinez, N. Xue, Z. Xiang, N.V. Thakor, C. Lee, IEEE Trans. Biomed. Eng. 63 (2016) 581–587.
[89] T.N. Nielsen, G.A. Kurstjens, J.J. Struijk, IEEE Trans. Biomed. Eng. 58 (2011) 913–919.
[90] L.D. Liao, M.L. Li, H.Y. Lai, Y.Y. Shih, Y.C. Lo, S. Tsang, P.C. Chao, C.T. Lin, F.S. Jaw, Y.Y. Chen, Neuroimage 52 (2010) 562–570.

Sanghoon Lee received the B.S.E. degree at the Department of Electronic Material Engineering, Kwangwoon University, Korea in 2009 and his M.S.E. degree at the Department of Electrical and Computer Engineering (ECE), National University of Singapore (NUS) in 2013. The research topic was the development of functional superparamagnetic nanoparticles for hyperthermia/MRI agents in nanomedicine. Currently, he is a Ph.D. candidate under Prof. Vincent C. Lee at the ECE in NUS as well as Assist. Prof. Shih-Cheng Yen in Singapore Institute for Neurotechnology (SINAPSE). His current research topic is the development of MEMS based neural prosthesis.

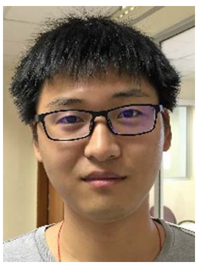

Hao Wang received his B.Eng. degree in School of Optoelectronic Information from University of Electronic Science and Technology of China in 2010. His Ph.D. degree is conferred in Electrical & Computer Eng. Dept., NUS in Oct 2016. Dr. Wang is currently employed as a Research Fellow in ECE, NUS. His research interests are focused on nanoneedle devices for transdermal drug delivery and triboelectric energy harvester.

Qiongfeng Shi received his B.Eng. degree from Department of Electronic Engineering and Information Science at University of Science and Technology of China (USTC) in 2012. He is currently pursuing his Ph.D. degree in the Department of Electrical and Computer Engineering, National University of Singapore (NUS) under the NUS research scholarship. His research interests are mainly focused on energy harvesters and self-powered sensors.

Lokesh Dhakar received his B.E. (Hons.) degree in Mechanical Engineering from Birla Institute of Technology and Science, Pilani in 2010. He worked in the industry as a design engineer from 2010 to 2011. He is currently working toward his Ph.D. degree from NUS Graduate School of Integrative Sciences and Engineering National University of Singapore, Singapore. He is also keenly interested in entrepreneurship and technology commercialization. He is currently working on energy harvesting devices aimed at powering wireless wearable sensors for healthcare.

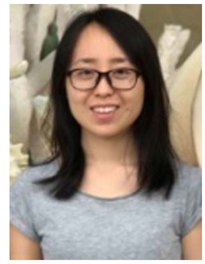

Jiahui Wang is currently a Ph.D. candidate in Department of Electrical & Computer Engineering, National University of Singapore. She received her Bachelor's degree in Department of Microelectronics, Fudan University in 2014. She is mainly interested in implantable neural interfaces, biocompatible sensors and energy applications.

Nitish V. Thakor is the Director the Singapore Institute for Neurotechnology (SINAPSE) at the National University of Singapore and the Professor of Electrical and Computer Engineering and Biomedical Engineering. Previously he was the Professor of Biomedical Engineering at Johns Hopkins University. Prof. Thakor's technical expertise is in the field of Neuroengineering, where he has pioneered many technologies for brain monitoring to prosthetic arms and neuroprosthesis. He is currently the Editor in Chief of Medical and Biological Engineering and Computing, and was the Editor in Chief of IEEE TNSRE from 2005 to 2011.

Shih-Cheng Yen received his B.S.E. and M.S.E. in 1993, and his Ph.D. in 1998, all from the Department of Bioengineering at the University of Pennsylvania. For his Ph.D., he worked on neural network models of the primary visual cortex. He was a Research Assistant Professor at Montana State University. He is currently an Assistant Professor in the Department of Electrical and Computer Engineering at the National University of Singapore (NUS), and the Deputy Director of the Singapore Institute for Neurotechnology (SINAPSE) at NUS. His research interests are in neural coding and neuroprosthetics.

Chengkuo Lee is the director of Center for Intelligent Sensors and MEMS at National University of Singapore. He received M.Sc. in Department of Materials Science & Engineer, National Tsing Hua University, Taiwan in 1991, M.Sc. in Department of Industrial & System Engineering, the State University of New Jersey, Rutgers, USA in 1993, and Ph.D. in Department of Precision Engineering, University of Tokyo, Japan in 1996. His research interests include energy harvesting, biomedical devices, flexible electronics, photonics, MEMS and NEMS.